

Abstract

Tidal oscillations of venting temperature and chlorinity have been observed in the long-term times-series data recorded by the Benthic and Resistivity Sensors (BARS) at the Grotto mound on the Juan de Fuca Ridge. In this study, we use a one-dimensional two-layer poroelastic model to conduct a preliminary investigation of three hypothetical scenarios in which seafloor tidal loading can modulate the venting temperature and chlorinity at Grotto through the mechanisms of subsurface tidal mixing and/or subsurface tidal pumping. For the first scenario, our results demonstrate that it is unlikely for subsurface tidal mixing to cause coupled tidal oscillations in venting temperature and chlorinity of the observed amplitudes. For the second scenario, the model results suggest it is plausible that the tidal oscillations in venting temperature and chlorinity are decoupled with the former caused by subsurface tidal pumping and the latter caused by subsurface tidal mixing, although the mixing depth is not well constrained. For the third scenario, our results suggest it is plausible for subsurface tidal pumping to cause coupled tidal oscillations in venting temperature and chlorinity. In this case, the observed tidal phase lag between venting temperature and chlorinity is close to the poroelastic model prediction if brine storage occurs throughout the upflow zone under the premise that layer 2A and 2B have similar crustal permeabilities. However, the predicted phase lag is poorly constrained if brine storage is limited to layer 2B as would be expected when its crustal permeability is much smaller than that of layer 2A.

1 Introduction

Mid-ocean ridge hydrothermal venting is the seafloor manifestation of buoyancy-driven circulation of aqueous fluid within the oceanic crust. Over the past several decades, a large number of studies have observed episodic and periodic variations in long-term monitoring of venting temperature, flow rate, and chemical compositions at both low and high temperature hydrothermal systems over a broad range of time scales [e.g., *Little et al.*, 1988; *Schultz et al.*, 1996; *Sohn et al.*, 1998; *Tivey et al.*, 2002; *Scheirer et al.*, 2006; *Larson et al.*, 2007, 2009; *Nees et al.*, 2009; *Crone et al.*, 2010; *Barreyre et al.*, 2014b]. In particular, spectral analysis has identified strong tidal signatures in hydrothermal venting in many of these studies. Among them, some attribute the observed tidal oscillations to the tidally-driven bottom currents, which can affect the temperature measured on or just beneath the surface of a hydrothermal sulfide by changing the thickness of the thermal boundary layer [*Little et al.*, 1988], advecting warm fluids from adjacent sources [*Tivey et al.*, 2002], or through conductive cooling of the sulfide deposit (proposed

52 by *Tivey et al.* [2002] to explain the tidal oscillations observed in the temperature measured
53 by a sensor buried in the sulfide deposit).

54 Alternatively, other studies interpret observed tidal oscillations, especially in measurements
55 of high temperature venting made inside the vent chimney, as the poroelastic response of crustal
56 fluids to seafloor tidal loading [e.g., *Larson et al.*, 2007, 2009; *Barreyre et al.*, 2014b; *Barreyre*
57 *and Sohn*, 2016]. Based on observations made at the Lucky Strike Hydrothermal Field on the
58 Mid-Atlantic Ridge, *Barreyre et al.* [2014b] suggested low-temperature venting (i.e., diffuse
59 flows) is mostly affected by bottom currents while high temperature venting (i.e., “black smokers”)
60 is mostly affected by tidal loading. Specifically, two different mechanisms have been proposed
61 to explain how tidal loading can perturb the temperature and chlorinity of high-temperature
62 hydrothermal effluents, which are discussed as follows.

63 The first mechanism is what we call subsurface tidal mixing. *Larson et al.* [2009] observed
64 tidal oscillations in both venting temperature and chlorinity at multiple high-temperature vents
65 in the Main Endeavour Field (MEF) on the Juan de Fuca Ridge. They interpret those tidal signatures
66 as the result of the tidally-driven subsurface mixing between high-chlorinity brine and low-
67 chlorinity vapor. We need to emphasize that the brine and vapor involved in the mixing process
68 discussed in their paper are different from the conjugate brine/vapor pair formed from phase
69 separation of heated seawater within the basal reaction zone of a hydrothermal circulation cell.
70 For the current study, brine and vapor refer broadly to fluids that are enriched and depleted
71 in chloride, respectively, compared to seawater. According to *Fontaine and Wilcock* [2006], as
72 a result of interfacial tensions, rising brine preferentially fills small fissures, dead ends, and
73 backwater porosity thereby covering the inner walls of the main conduits through which vapor
74 flows (Figure 3(b)(c)). This is because brine is denser and thus forms a higher density of hydrogen
75 bonds and likely contains a higher proportion of free ions that will enhance the adhesion of
76 brine to rock compared to vapor. Under tidal loading, incremental pore pressure compresses
77 the volume of highly compressible vapor and squeezes the adjacent less-compressible brine
78 into the pore space to fill the void, resulting in the addition of small amounts of brine to vapor-
79 dominated fluid. Such tidally-driven mixing causes the temperature and chlorinity of the vapor
80 to vary at tidal frequencies within the subsurface mixing zone. Those variations eventually show
81 up at vent orifices as the vapor reaches the seafloor.

82 The second mechanism is what we call subsurface tidal pumping. According to *Jupp and*
83 *Schultz* [2004b], under periodic tidal loading, the varying pore pressure gradient perturbs the

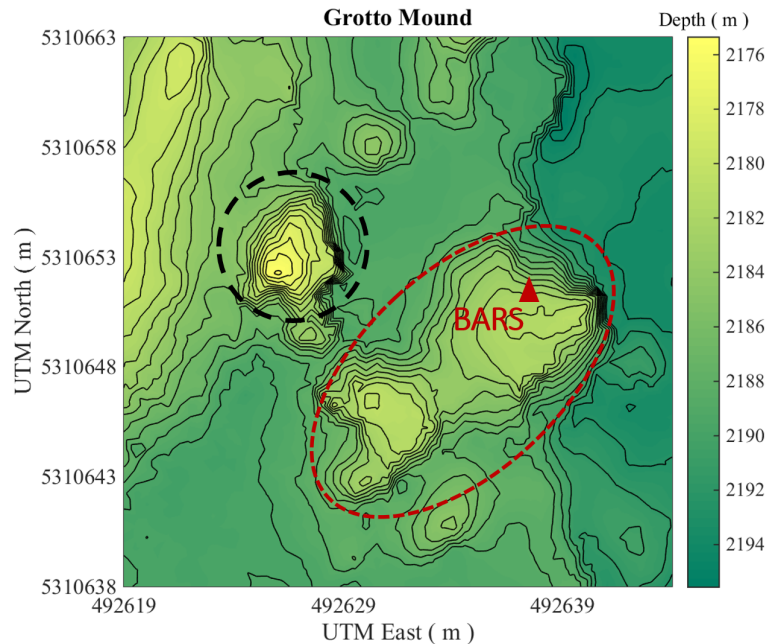
84 flow rate at which hydrothermal fluid ascends along the subsurface discharge zone to oscillate
85 at tidal frequencies. Furthermore, conductive and adiabatic cooling leads to a vertical temperature
86 gradient throughout the discharge zone. As a result, the oscillating flow velocity of ascending
87 hydrothermal fluid causes displacement of the vertical temperature gradient near the seafloor,
88 which then causes the venting temperature to vary at tidal frequencies. As discussed later in
89 this paper, the same mechanism can also lead to tidal oscillations of venting chlorinity assuming
90 a vertical chlorinity gradient is maintained along the discharge zone by diffusion of chloride
91 from brine to vapor.

92 In this paper, we investigate tidal oscillations observed in time-series of venting temperature
93 and chlorinity recorded at the Grotto mound in the MEF from June 2013 to Jan 2014. We use
94 a one-dimensional two-layer poroelastic model and equations of state applicable to the range
95 of temperature, chlorinity, and pressure within the subsurface hydrothermal discharge zone to
96 test three hypotheses concerning the mechanism for tidal oscillations in focused vents: 1) subsurface
97 tidal mixing causes coupled tidal oscillations in venting temperature and chlorinity [*Larson*
98 *et al.*, 2009], 2) tidal oscillations in temperature and chlorinity are decoupled, with temperature
99 variations originating from subsurface tidal pumping, and chlorinity variations originating from
100 subsurface tidal mixing, and 3) subsurface tidal pumping causes coupled tidal oscillations in
101 venting temperature and chlorinity.

102 **2 Study Site**

103 Grotto mound, is a large venting sulfide structure (area $\sim 450\text{ m}^2$) within the Main Endeavour
104 Field on the Endeavour Segment of the Juan de Fuca Ridge. Grotto consists of an edifice with
105 NE-SW major axis in the east and a 10 m tall edifice near the western rift valley wall (Figure
106 1). Grotto is one of the most hydrothermally active structures in the MEF. The elliptical and
107 cylindrical edifices each hosts several “black smokers” with diffuse flows percolating through
108 areas around those smokers. The Grotto mound is also a major study site of the MEF node
109 of the NEPTUNE observatory operated by Ocean Networks Canada. The observatory connects
110 multi-disciplinary instruments located on or near Grotto that monitor the local hydrothermal,
111 oceanic, geological, and biological activities [*Kelley et al.*, 2014]. Among those instruments,
112 the Benthic and Resistivity Sensors (BARS) — which measure temperature, chlorinity, and
113 oxidation-reduction potential (Eh) inside the throat of a “black smoker” on the elliptical edifice
114 (Figure 1) — is the primary source of the observational data presented in this paper. The contemporaneous

115 seafloor pressure data was recorded by an acoustic Doppler current profiler (ADCP) at approximately
 116 80 m to the south of Grotto.

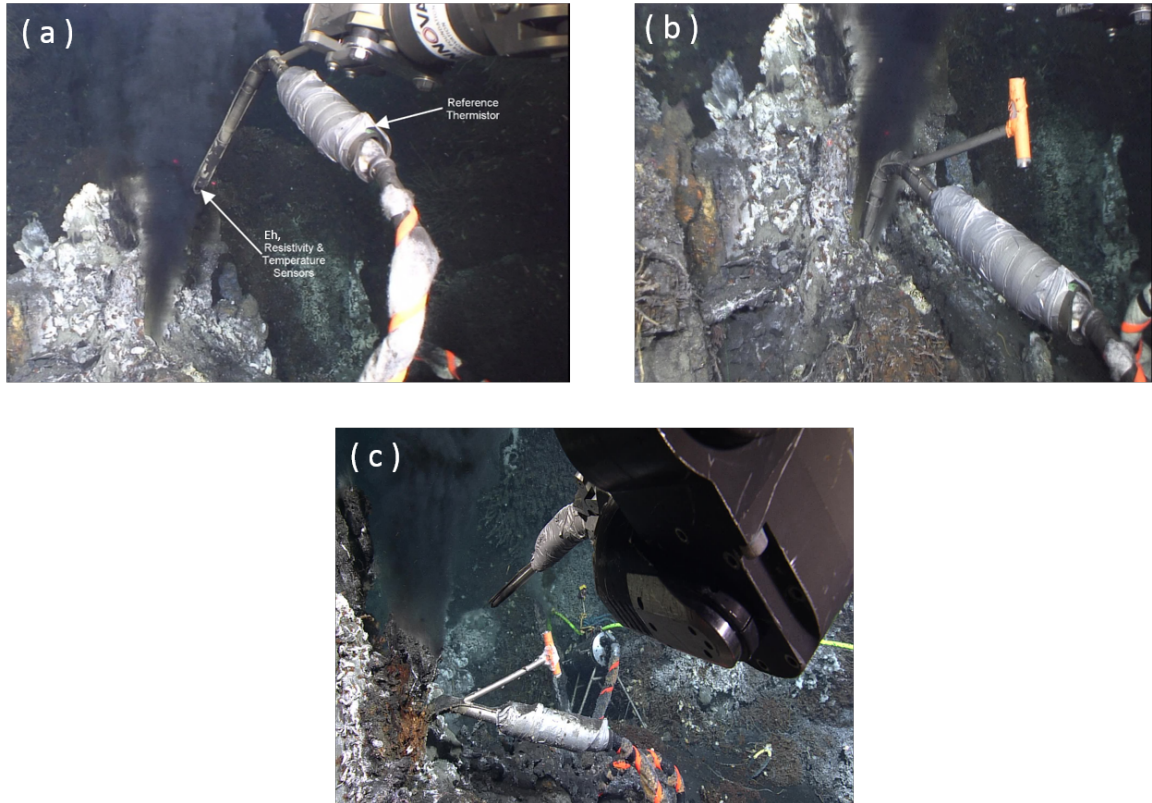


117 **Figure 1.** Bathymetric map of the Grotto mound. The contour line interval is 1 m. The black and red
 118 dashed lines delimit the areas of Grotto's two major edifices, respectively. The red triangle marks the location
 119 of the Benthic and Resistivity Sensors (BARS). The bathymetric data used to produce the map was collected
 120 during an AUV survey in 2008 with ~ 1 m lateral resolution and ~ 0.1 m vertical resolution [Clague *et al.*,
 121 2008, 2014].

122 3 Methods

123 3.1 Instrumentation and Data Collection

124 The BARS instrument package used for this study is detailed in *Larson et al.* [2007] with
 125 modifications as described by *Larson* [2008]. The package includes a high-temperature sensor,
 126 a resistivity sensor, an Eh sensor, and a reference-temperature sensor. The high-temperature,
 127 Eh, and resistivity sensors are located at the end of a L-shaped titanium wand with 20 cm after
 128 the elbow intended for submersion in a high-temperature sulfide. The reference-temperature
 129 sensor is located at the other end of wand in ambient conditions (Figure 2a).



130 **Figure 2.** (a) Installation of BARS wand into a high temperature vent at the Grotto mound. The photo
131 was taken on June 18th, 2013 at 22:13:06 UTC. The sensor locations are marked in the photo. The reference
132 thermistor is located near the rear end of the L-shaped wand inside the rubber boot covered in duct tape,
133 and the arrow only gives its general location. (b) Close up view of deployed wand just after installation.
134 Approximately 2 grooves in the wand are visible, with the third just below the lip of the chimney. The photo
135 was taken approximately 25 min after (a). (c) View of gas tight sampling (top instrument held by the ROV
136 manipulator) in chimney where BARS was deployed 11 months earlier. The photo was taken on May 18th,
137 2014 at 22:21:51 UTC. At this time, the chimney has sealed the entire wand and continued to grow on top of
138 it.

157 **Table 1.** Sample and Sensor Data for Conductivity-to-chlorinity Conversion

Description	Pre-Deployment	During Deployment
Sample Date (UTC)	18-June-2013 14:57	18-May-2014 22:20
End-member Chlorinity (mmol/kg)	497.5 ¹	435.8
Data used for comparison with sample (UTC)	18-June-2013 22:55-23:02	18-May-2014 22:21-22:27
Avg. Temperature (°C)	332.7	335.6
Avg. Conductivity (V ⁻¹)	1.41	1.51

¹ Average of 2 samples with 1.3% difference

139 The depth of penetration of the high temperature end can be approximated using grooves
140 in the wand that are spaced approximately 2.5 cm apart. Based on pictures of the deployed
141 wand (Figure 2b), ~ 5 cm of the back end of the wand is exposed, suggesting ~ 15 cm of
142 penetration into the sulfide. Pictures taken 11 months after the deployment show the wand is
143 completely cemented in place up to the elbow, and approximately 10 cm of new chimney has
144 formed on top (Figure 2c). These pictures imply BARS is sensing high-temperature flow that
145 is isolated from the ambient seawater and bottom currents throughout its deployment.

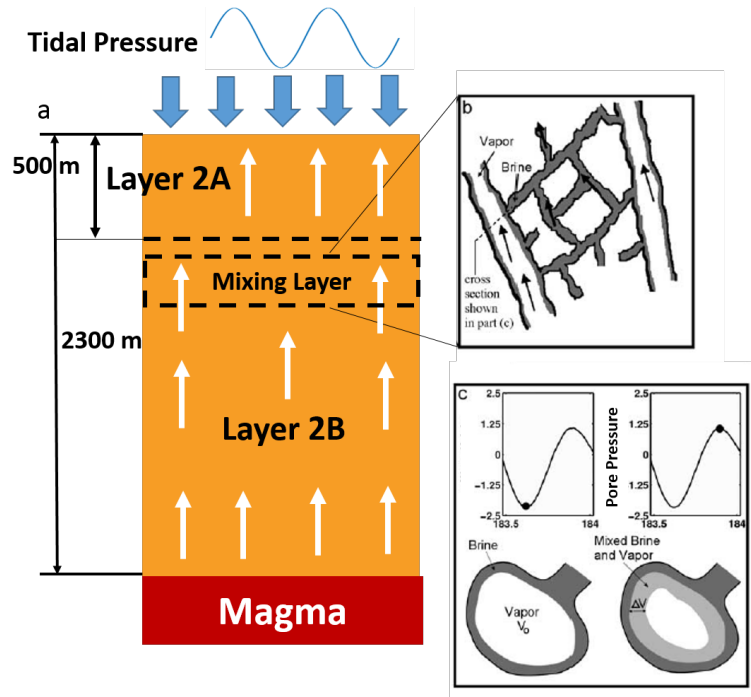
146 Calibrated temperature values were directly downloaded from Ocean Networks Canada
147 (ONC) database [*Ocean Networks Canada Data Archive*, 2014b], and details of the calibration
148 formula can be found at <https://wiki.oceannetworks.ca/display/instruments/15002>. For chloride
149 concentrations, resistivity values were first downloaded from the ONC database [*Ocean Networks*
150 *Canada Data Archive*, 2014a], then the reciprocal taken to give conductivity values in V⁻¹ (here
151 and elsewhere, conductivity refers to the inverse of the resistivity measured in volts). Finally,
152 we converted conductivity to chloride concentration using the method described in *Larson et al.*
153 [2007] in conjunction with the Temperature-Conductivity-NaCl surface shown in *Larson* [2008]
154 and average chloride concentration from discrete fluid samples taken prior to and part-way through
155 the BARS deployment (Table 1). The resulting temperature and chlorinity time series have a
156 sampling period of 20 seconds.

3.2 Poroelastic Model

The pressure of the crustal pore fluid hosted by seafloor formations varies in response to tidal loading on the seafloor. Such response includes an instantaneous pore pressure change at all depths and a diffusive pressure change that propagates from the seafloor into the formation and across internal layer boundaries [Wang and Davis, 1996; Jupp and Schultz, 2004b]. Both instantaneous and diffusive pore pressure variations are dependent on the poroelastic properties of both the pore fluid and the crustal matrix framework. Pore pressure variations are governed by equations of poroelasticity, which have been used in many studies to investigate sub-seafloor pore pressure variations and their role in fluid flow response to tidal loading and geological events [Wang and Davis, 1996; Davis et al., 2000, 2001; Jupp and Schultz, 2004b; Barreyre et al., 2014a; Barreyre and Sohn, 2016]. In this study, we use the one-dimensional multilayer poroelastic model developed by Wang and Davis [1996] to predict the tidally induced pore pressure variations beneath the MEF. Appendix A gives the model equations.

The hydrothermal circulation system consists of a broad recharge zone (presumably primarily on axis), fluid heated at the base of the sheeted dikes just above the axial magma chamber (AMC), and a focused upflow zone [e.g., Fontaine and Wilcock, 2006; Coogan, 2008; Coumou et al., 2009]. Based on the seismic study of Van Ark et al. [2007], the hydrothermal upflow zone beneath the MEF is represented in the model as a poroelastic medium comprising the typical seismic layers 2A and 2B of zero-age oceanic crust (Figure 3). The crustal properties are homogeneous within layers but differ between them. The top boundary of the model is the seafloor, which is open to fluid flow. The bottom boundary of the model is the ceiling of the axial magma chamber (AMC) and is closed to fluid flow. The depths of the layer 2A/2B interface and the AMC are constrained by the seismic observations of Van Ark et al. [2007]. Table 2 gives the values of those depths along with other crustal and fluid properties used in the model. Matrix bulk modulus K_m , fluid bulk modulus K_f , and crustal permeability k are three primary parameters governing the response of the seafloor formation to tidal loading. The matrix bulk modulus K_m is the bulk modulus of the crustal matrix framework when its pore space is empty. In practice, we calculate K_m using Gassmann's equation given in Jupp and Schultz [2004b].

Compared with other properties, the crustal permeability k and the fluid bulk modulus K_f are most poorly constrained, particularly the former. For the Endeavour Segment, Hearn et al. [2013] estimated the surface permeability to be $k \sim 10^{-11} - 10^{-10} \text{ m}^2$ based on high-resolution seafloor photomosaics. Additionally, those authors estimated sub-surface permeability



186 **Figure 3.** (a) Schematic of the crustal structure within the hydrothermal discharge zone in the one-
 187 dimensional two-layer poroelastic model. The hypothesized subsurface mixing between brine and vapor
 188 occurs within a thin layer beneath the layer 2A/2B interface. (b) cartoon of brine and vapor distribution within
 189 the mixing zone modified from *Fontaine and Wilcock* [2006]. (c) Cartoon illustrating the subsurface mixing
 190 between brine and vapor under tidal loading reproduced from *Larson et al.* [2009]. The incremental pore
 191 pressure caused by seafloor loading compresses the vapor flowing through a major conduit and squeezes the
 192 adjacent less compressible brine into the void.

Table 2. Symbols and Values of Parameters

Symbol	Description	Values and Units
k	crustal permeability	m^2
K_f	fluid bulk modulus	Pa
β_f	fluid compressibility (K_f^{-1})	Pa^{-1}
K_m	matrix bulk modulus	$6.1 \times 10^9 \text{ Pa}$ (layer 2A), $4.8 \times 10^9 \text{ Pa}$ (layer 2B)
S_b	chlorinity of brine	mmol/kg
S_v	chlorinity of vapor	mmol/kg
T_f	temperature of pore fluid	$40 \text{ }^\circ\text{C}$ (layer 2A), $370 \text{ }^\circ\text{C}$ (layer 2B)
T_b	temperature of brine	$^\circ\text{C}$
T_v	temperature of vapor	$^\circ\text{C}$
ϕ	crustal porosity [<i>Crone and Wilcock, 2005</i>]	0.2 (layer 2A), 0.03 (layer 2B)
ρ_0	density of cold background pore fluid	1000 kg/m^3
ρ_v	density of vapor	kg/m^3
ρ_b	density of brine	kg/m^3
μ	fluid dynamic viscosity	$8.3 \times 10^{-5} \text{ Pa} \cdot \text{s}$
Σ	1-D storage compressibility	$2.1 \times 10^{-10} \text{ Pa}^{-1}$ (layer 2A), $1.5 \times 10^{-10} \text{ Pa}^{-1}$ (layer 2B)
γ	1-D Skempton ratio	0.65 (layer 2A), 0.03 (layer 2B)

198 to be $k \approx 2.5 \times 10^{-12} - 2 \times 10^{-10} \text{ m}^2$ for layer 2A and $k \approx 4.0 \times 10^{-15} - 7.9 \times 10^{-13} \text{ m}^2$ for
 199 layer 2B based on a linear relationship between permeability and measured seismic velocity
 200 [Carlson, 2011; Newman *et al.*, 2011; Nedimovi *et al.*, 2008]. Most recently, Barreyre and Sohn
 201 [2016] estimated layer 2A permeability at Grotto to be $2.5 \times 10^{-13} \text{ m}^2$ based on phase angles
 202 of the tidal oscillations in venting temperature and the assumption that subsurface tidal pumping
 203 is the causal mechanism for those tidal variations. Alternatively, Wilcock and McNabb [1996]
 204 and Lowell *et al.* [2013] estimated the uniform crustal permeability to be $k \sim 10^{-13} - 10^{-12} \text{ m}^2$
 205 using mathematical models of hydrothermal convection constrained by observations of the spatial
 206 distribution and heat output of hydrothermal venting at Endeavour. Combining the estimates
 207 above, we take the ranges of k as: $10^{-13} - 10^{-10} \text{ m}^2$ for layer 2A and $10^{-15} - 10^{-12} \text{ m}^2$
 208 for layer 2B.

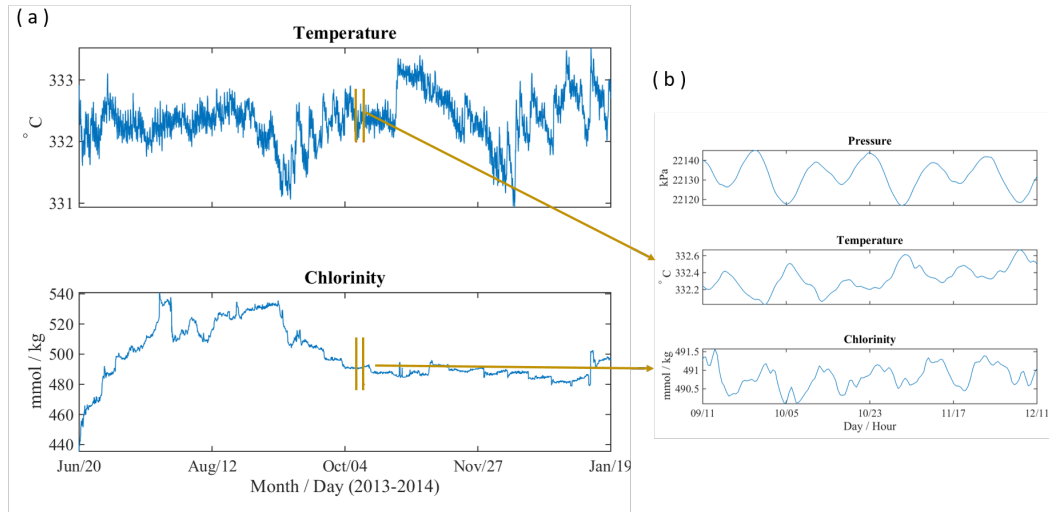
209 The fluid bulk modulus K_f or its reciprocal, compressibility β_f , is largely determined
 210 by fluid temperature T_f . Although the venting temperature at Grotto is recorded by BARS at
 211 $\sim 332^\circ\text{C}$ on the seafloor (Figure 4), the subsurface temperature is not as well constrained
 212 and can significantly exceed the surface measurements. This is because the temperature of “black
 213 smoker” fluid decreases during its ascent as a result of conductive heat loss and adiabatic decompression.
 214 Jupp and Schultz [2000] and Jupp and Schultz [2004a] used a convection model to predict that
 215 hydrothermal fluid, constrained by the non-linear thermodynamic properties of water, may be
 216 close to a temperature of 400°C near the subsurface heat source. In practice, we set $T_f =$
 217 370°C , which is approximately midway between the seafloor temperature measurement (332°C)
 218 and the estimated subsurface maximum (400°C). We then calculate the pore fluid compressibility
 219 using the equation of state developed by Driesner [2007] for 370°C 2.85 Wt.% (489 mmol/kg)
 220 NaCl solution at a reference pressure of $3.35 \times 10^4 \text{ kPa}$. The chlorinity is chosen as the average
 221 BARS measurements over a relatively steady period between Oct 10 and 25, 2013. The reference
 222 pressure assumes cold hydrostatic and is calculated at a depth midway between the seafloor
 223 and the bottom of the discharge supply conduit.

224 **4 Results**

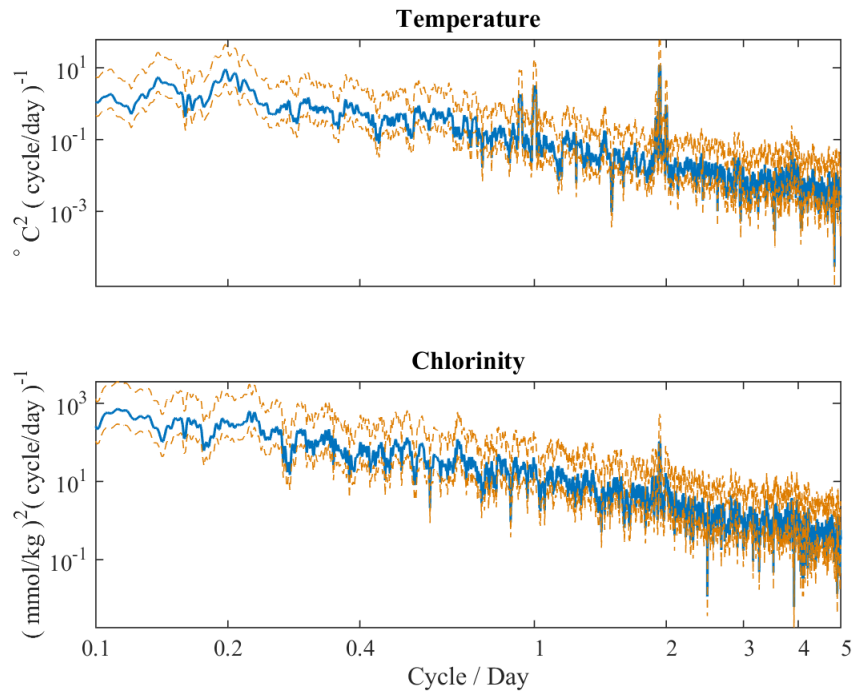
225 **4.1 BARS Data Analysis**

226 Vent temperature and chlorinity data used in this study were recorded by Benthic And
 227 Resistivity Sensors (BARS) during its deployment at Grotto between June 2013 and Jan 2014
 228 (Figure 4). During the seven month period shown in Figure 4(a), temperature fluctuates between

229 330.5 and 333.9 °C with a mean value of 332 °C and a standard deviation of 0.42 °C. In comparison,
230 chlorinity shows more pronounced variations, which are from 433 to 544 mmol/kg with a mean
231 value of 500 mmol/kg and a standard deviation of 17.6 mmol/kg. The standard deviation to
232 mean ratio for temperature and chlorinity are 0.1% and 3.5% respectively. The zoom-in view
233 of a 3-day period from Oct 9 to 12, 2013 shows periodic oscillations at semi-diurnal frequency
234 (twice a day) for both temperature and chlorinity (Figure 4(b)). Figures 5(a)(b) show the power
235 spectra of temperature and chlorinity time series data obtained using the multi-taper method
236 [Thomson, 1982] with adaptive weighting [Percival and Walden, 1993]. The spectrum of temperature
237 has significant peaks within the diurnal and semi-diurnal tidal frequency bands with the principal
238 lunar semi-diurnal constituent (M2) being the dominant tidal frequency. In comparison, the
239 spectrum of chlorinity has a significant peak at M2 tidal frequency but shows no indication
240 of the presence of diurnal tidal signals. Given that the dominant tidal constituent in both temperature
241 and chlorinity is M2, we use it as the primary tidal signal for the data analysis described in
242 the rest of the paper. To obtain more details of the M2 tidal oscillations (e.g., amplitude, phase
243 angle, phase lag relative to tidal pressure), we conducted harmonic analysis on the time series
244 of temperature and chlorinity shown in Figure 4 along with seafloor pressure measured by the
245 ADCP at approximately 80 m to the south of Grotto using the harmonic analysis toolbox T-
246 Tide developed by Pawlowicz *et al.* [2002]. Table 3 shows the results.



247 **Figure 4.** (a) Time series of hourly averaged venting temperature (upper panel) and chlorinity (lower panel)
 248 recorded by BARS at Grotto from Jun 2013 to Jan 2014. (b) Zoom-in view of a three-day period delimited by
 249 the vertical lines in (a) of venting temperature (middle panel) and chlorinity (lower panel) along with seafloor
 250 pressure measured by the ADCP (top panel).



251 **Figure 5.** (a) Power spectral density of the time series of venting temperature recorded at Grotto between
 252 June 2013 and January 2014 (blue). The dashed brown curves delimit the 95% confidence interval. (b) Same
 253 as (a) but for chlorinity.

254

Table 3. Harmonic Analysis Results

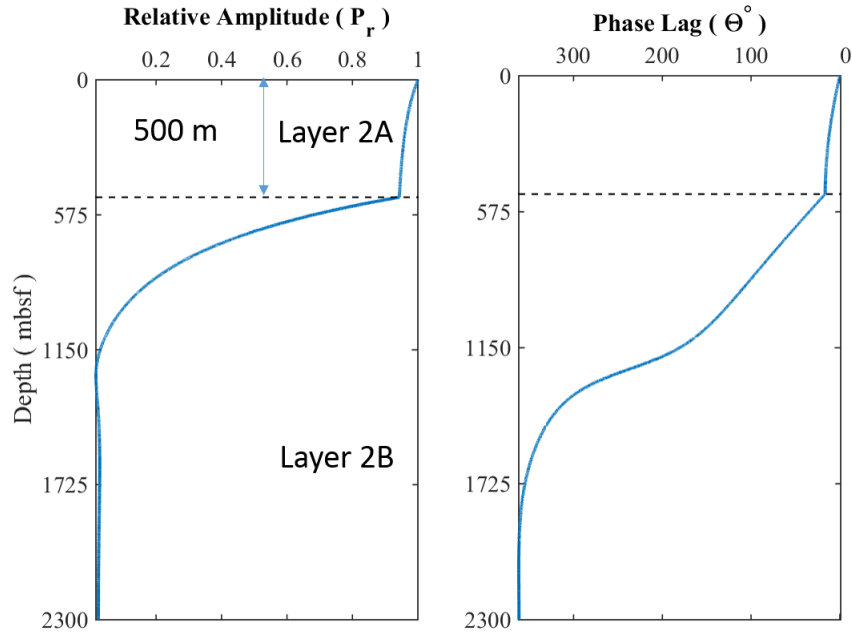
	Amplitude	Phase	1/2 95% CI	phase lag w.r.t M2 tide
M2 (semi-diurnal) tide	9 kPa	241°	0.28°	0
Temperature	0.12 °C	97.1°	1.82°	216.1 ± 2.1°
chlorinity	0.34 mmol/kg	299.9°	8.82°	58.9 ± 9.1°
phase lag of chlorinity w.r.t. temperature: 202.8 ± 10.6°				
K1 (diurnal) tide	4.3 kPa	242°	0.57°	1 ± 0.85°
Temperature	0.06 °C	77.1°	7.16°	195.1 ± 7.73°
Chlorinity	0.2 mmol/kg	251.9°	30.86°	9.9 ± 31.43°

255 Note that the lack of diurnal peak in the spectrum of chlorinity is likely because the amplitude
256 of the diurnal oscillations in chlorinity is small and thus buried in the ambient noise in the spectrum.
257 The formulas given in Appendices A and B suggest the amplitudes of tidal harmonics in temperature
258 and chlorinity should be approximately proportional to the amplitudes of the corresponding
259 loading tides. As shown in Table 3, the amplitude of the diurnal tide (4.3 kPa) is approximately
260 one half of that of the semi-diurnal tide (9 kPa). The diurnal harmonic ($K1$) in venting temperature
261 (0.06 °C) is indeed one half of its semi-diurnal harmonic (0.12 °C) (Table 3) and the diurnal
262 peak appears roughly half the size of the semi-diurnal peak in Figure 5. Despite the lack of
263 a visible diurnal peak, the amplitude of the diurnal harmonic ($K1$) in chlorinity estimated using
264 T-Tide is 0.20 mmol/kg, which is also close to one half of the semi-diurnal harmonic (0.34
265 mmol/kg) (Table 3). Therefore, it is likely that subsurface tidal pumping causes chlorinity oscillations
266 at both diurnal and semi-diurnal frequencies, and that the former is simply below the noise
267 threshold of the power spectrum.

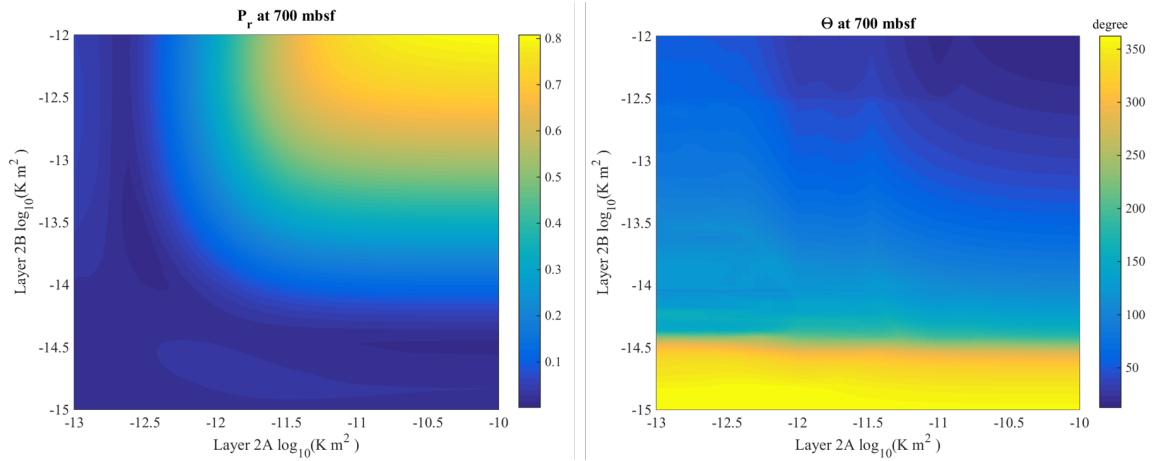
268 4.2 Subsurface Pore Pressure Variations

269 We estimate the amplitudes and phase angles associated with the subsurface pore pressure
270 variations under a tidal loading at M2 frequency using the poroelastic model discussed in Section
271 3.2 and Appendix A. Figure 6 shows the result obtained using intermediate crustal permeabilities:
272 $k = 5 \times 10^{-12} \text{ m}^2$ for layer 2A and $5 \times 10^{-14} \text{ m}^2$ for layer 2B and constant fluid compressibility
273 for 370 °C 2.85 Wt.% (489 mmol/kg) NaCl solution at a reference pressure of 3.35×10^4

274 kPa. According to Figure 6, the relative amplitude (P_r), which is the ratio of the pore pressure
275 amplitude to the seafloor pressure amplitude, decreases with increasing depth beneath the seafloor.
276 The decrease is minimal within layer 2A ($\sim 5\%$ at the interface) due to its large permeability,
277 which leads to fast downward interstitial flow that propagates the seafloor pressure signal through
278 the layer without significant loss of amplitude. Within layer 2B, the relative amplitude decreases
279 exponentially towards a small but non-zero constant—the Skempton ratio, which is the proportion
280 of the seafloor loading that is borne by the pore fluid in the absence of interstitial fluid flows
281 [Jupp and Schultz, 2004b]. At 700 mbsf, the value of P_r is 0.39. The phase lag (θ) of the pore
282 pressure variations relative to seafloor loading increases with depth, and the increase is minimal
283 within Layer 2A ($\theta \sim 3^\circ$ at the Layer 2A/2B interface). Such a small phase lag is also due
284 to the large permeability of Layer 2A and the resulting fast interstitial flow that propagates the
285 seafloor pressure signal through the layer without much delay. Within layer 2B, θ increases
286 rapidly, reach near 360° (zero) by a depth of 1800 m with the permeability and fluid compressibility
287 used. At 700 mbsf, the phase lag is $\theta = 64^\circ$. Figure 7 shows the variations of P_r and θ at
288 700 mbsf as functions of layer 2A and 2B permeabilities. According to Figure 7, P_r increases
289 with increasing permeabilities of both layers and is more sensitive to the permeability of layer
290 2B. In contrast, θ decreases with increasing permeabilities of both layers and is also more sensitive
291 to the permeability of layer 2B.



292 **Figure 6.** Relative amplitude (left) and phase lag (right) of pore pressure oscillations under seafloor loading
 293 of M2 tide predicted by the poroelastic model using base-line crustal permeabilities: $k = 5 \times 10^{-12} \text{ m}^2$
 294 for layer 2A and $5 \times 10^{-14} \text{ m}^2$ for layer 2B and constant fluid compressibility for 370 °C 2.85 Wt.% (489
 295 mmol/kg) NaCl solution at a reference pressure of $3.35 \times 10^4 \text{ kPa}$.



296 **Figure 7.** Predicted relative amplitude (left) and phase lag (right) of pore pressure oscillations
 297 under seafloor loading of M2 tide at 700 mbsf as functions of crustal permeabilities with constant fluid
 298 compressibility for 370 °C 2.85 Wt.% (489 mmol/kg) NaCl solution at a reference pressure of 3.35×10^4
 299 kPa.

4.3 Coupled Tidal Oscillations of Temperature and Chlorinity from Subsurface Tidal Mixing

As hypothesized by *Larson et al.* [2009], the tidal oscillations in venting temperature and chloride may originate from the subsurface tidal mixing between brine and vapor at depths where the vapor is close to its critical point and thus highly compressible. In order to test this hypothesis, we estimate the brine temperature and chlorinity and vapor compressibility needed to generate temperature and chlorinity oscillations of the observed amplitudes.

For modeling purposes, we assume the chlorinity of the vapor to be $S_v = S_0 - A_s = 488.5$ mmol/kg or 2.85 Wt.%, where $S_0 = 488.8$ mmol/kg is the time average of the chlorinity recorded over a relatively steady period from Oct 10 to 25, 2013 (Figure 4) and $A_s \approx 0.3$ mmol/kg is the amplitude of the M2 tidal oscillations in chlorinity (Table 3). The corresponding critical temperature and pressure of a NaCl solution with the same chlorinity are $\sim 400^\circ\text{C}$ and $\sim 2.9 \times 10^4$ kPa respectively [*Driesner and Heinrich, 2007*]. The critical pressure corresponds to approximately 700 m beneath the MEF, which is thus assumed to be the primary depth at which the subsurface mixing occurs. In addition, we also assume the temperature of the near-critical vapor to be 400°C . Note that this is different from the vapor temperature used in the poroelastic model (370°C) as the latter is considered the average over the discharge zone and hence more suitable to use in the model that assumes constant fluid properties.

As mentioned in Section 1, the increased pore pressure under tidal loading compresses the volume filled by the highly compressible near-critical vapor and squeezes the adjacent brine into the pore space to fill in the void. We can then estimate the volume fraction of brine (η_b) and vapor (η_v) in the mixing process as

$$\eta_b = \Delta P \beta_f \quad (1)$$

where ΔP is the incremental pore pressure and β_f is the compressibility of the near-critical vapor. In practice, we determine ΔP as the product of the relative amplitude of pore pressure oscillations (P_r) predicted by the poroelastic model (Figure 7) and the amplitude of the M2 oscillations in seafloor pressure estimated from harmonic analysis ($A_P = 9$ kPa, Table 3). In addition, we assume β_f to vary from 10^{-7} to 10^{-6} Pa $^{-1}$. The purpose of using this arbitrary range, which is independent of vapor temperature (400°C), is to obtain a hypothetical minimum vapor compressibility that is required to explain the observed tidal oscillations of temperature and chlorinity as discussed in the following.

330 Assuming mass, heat, and chloride are conserved during mixing leads to the following
 331 equations

$$\eta_v \rho_v + \eta_b \rho_b = \epsilon \rho_m, \quad (2)$$

$$\chi_v H_v + \chi_b H_b = H_m. \quad (3)$$

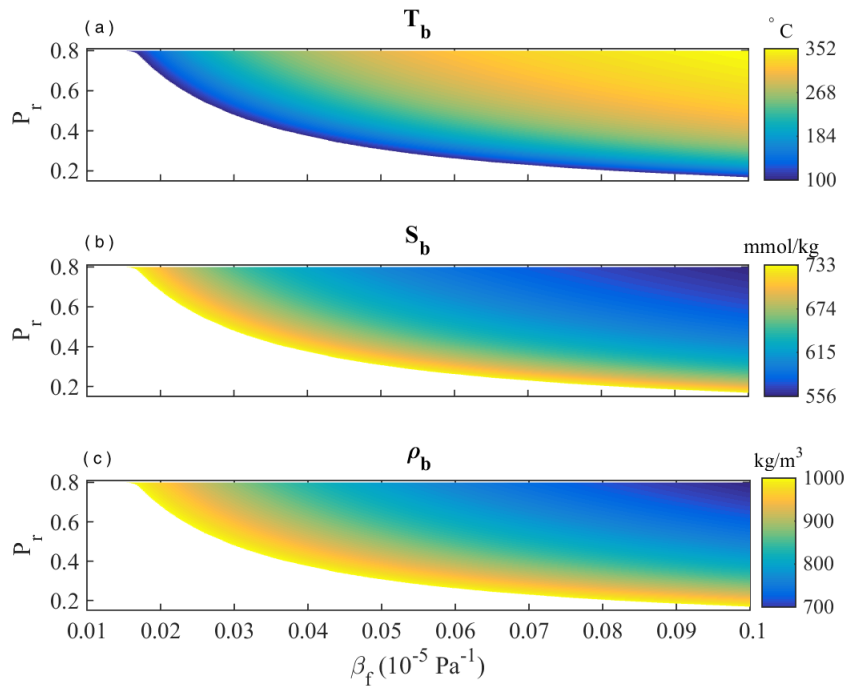
$$\chi_v S_v + \chi_b S_b = S_m, \quad (4)$$

332 Equation (2) represents the conservation of mass, where ρ is the fluid density and the subscripts
 333 v , b , m refer to vapor, brine, and mixture; ϵ is a constant coefficient used to compensate for
 334 the non-conserved nature of fluid volume during mixing. From equation (2), we derive the mass
 335 fractions of vapor and brine as $\chi_v = (\eta_v \rho_v) / (\epsilon \rho_m)$ and $\chi_b = 1 - \chi_v$. Equations (3) and (4)
 336 represent the conservation of heat and chloride respectively, where H and S are enthalpy and
 337 chlorinity.

338 In general, one can solve equations (2) to (4) to obtain the temperature and chlorinity
 339 of brine using the temperatures and chlorinities of vapor and mixture along with the formulas
 340 to calculate enthalpy and density as functions of temperature, chlorinity, and pressure. In our
 341 modeling, we determine the temperatures and chlorinities of vapor and mixture as follows. First,
 342 we assume the mixture is a result of colder brine mixing with hotter vapor. As discussed in
 343 the beginning paragraph of this section, we assume the temperature and chlorinity of vapor
 344 to be $T_v = 400^\circ\text{C}$ and $S_v = 448.5$ mmol/kg. We then determine the temperature of mixture
 345 as $T_m = T_v - 2A_T = 399.8^\circ\text{C}$ where $A_T \approx 0.1^\circ\text{C}$ is the amplitude of the M2 tidal oscillations
 346 in temperature (Table 3). Similarly, we determine the chlorinity of mixture as $S_m = S_v +$
 347 $2A_S = 449.1$ mmol/kg. Additionally, we use the formulas given in *Driesner* [2007] to calculate
 348 vapor and mixture enthalpy and density as functions of temperature and chlorinity at $2.9 \times$
 349 10^4 kPa. After obtaining brine enthalpy by solving equations (2) to (4), we convert it to brine
 350 temperature inversely based on the enthalpy formula given in *Driesner* [2007].

351 Figure 8 shows the temperature (T_b), chlorinity (S_b), and density (ρ_b) of brine obtained
 352 with vapor compressibility (β_f) varying from 10^{-7} to 10^{-6} Pa $^{-1}$ and $P_r = 0.1$ to 0.8 . The
 353 lower limit of P_r correspond to the pore pressure variations at 700 mbsf predicted by the poroelastic
 354 model with crustal permeabilities of $K = 8.1 \times 10^{-12}$ m 2 for layer 2A and $K = 8.6 \times$
 355 10^{-15} m 2 for layer 2B. The upper limit of P_r corresponds to $K = 9.1 \times 10^{-11}$ m 2 for layer
 356 2A and $K = 9.1 \times 10^{-13}$ m 2 for layer 2B. According to Figure 8, at fixed P_r , T_b increases

357 with increasing β_f while S_b and ρ_b follow the opposite trend. At fixed β_f , T_b increases with
 358 increasing P_r and the opposite applies to S_b and ρ_b . Also notice the cutoff of brine density
 359 at $\rho_b = 1000 \text{ kg/m}^3$. Such a cutoff density is chosen based on the assumption that the pressure
 360 gradient within the lower hydrothermal discharge zone in layer 2B is close to cold hydrostatic
 361 [Jupp and Schultz, 2004a; Fontaine and Wilcock, 2006] and thus only brines with density lower
 362 than that of the cold pore fluid ($\sim 1000 \text{ kg/m}^3$) will rise from the basal reaction zone and
 363 reach 700 mbsf. Consequently, Figure 8 suggests the minimum vapor compressibility required
 364 to interpret the tidal oscillations of temperature and chlorinity is $\beta_f = 1.9 \times 10^{-7} \text{ Pa}^{-1}$ at
 365 $P_r = 0.8$. This minimum increases to $\beta_f = 10^{-6} \text{ Pa}^{-1}$ at $P_r = 0.14$.



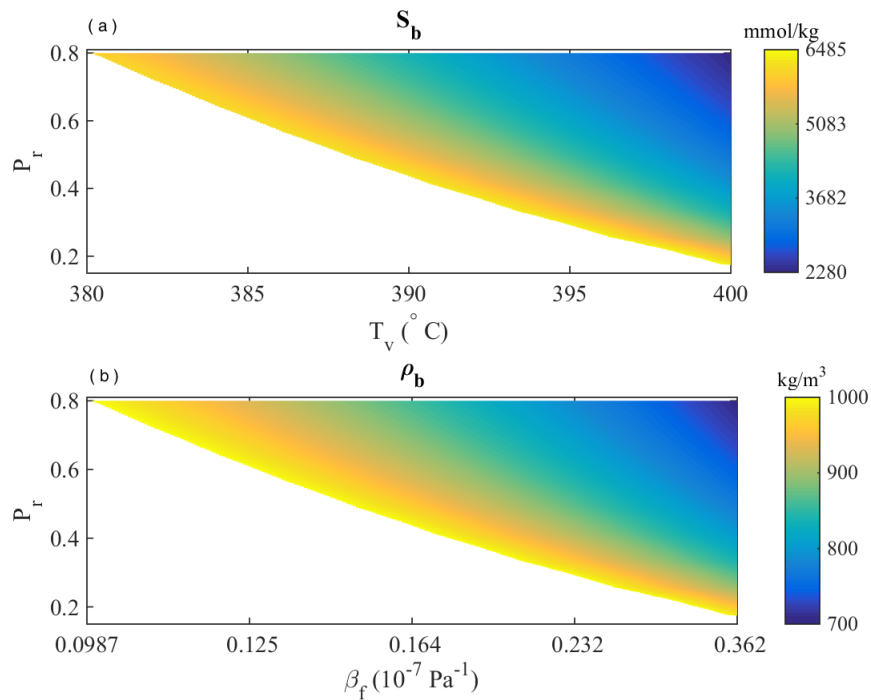
366 **Figure 8.** Estimated brine properties from coupled temperature and chlorinity tidally oscillations caused
 367 by subsurface tidal mixing: temperature (top), chlorinity (middle), and density (bottom) as functions of vapor
 368 compressibility (β_f) and relative amplitude of pore pressure oscillations (P_r). The results are cropped at the
 369 presumed maximum brine density of 1000 kg/m^3 .

370 4.4 Decoupled Tidal Oscillations of Temperature and Chlorinity

371 The results shown in Section 4.3 are obtained based on the premise that subsurface tidal
 372 mixing causes the tidal oscillations in both venting temperature and chloride. Alternatively,

373 it is plausible that the tidal signatures in temperature and chloride are decoupled and originate
 374 from separate causal mechanisms. For example, as discussed in Section 1, subsurface tidal pumping
 375 can be an alternative causal mechanism for the tidal oscillations observed in venting temperature.

376 To test the hypothesis that subsurface tidal mixing causes the tidal oscillations in venting
 377 chlorinity alone, we redo the calculations described in Section 4.3 by solving equations (2)
 378 to (4) under the condition of $T_v = T_b$ for mixing between brine and vapor in thermal equilibrium.
 379 We also assume subsurface mixing remains restricted to 700 mbsf. Figure 9 shows estimated
 380 brine chlorinity (S_b) and density (ρ_b) varying as functions of vapor temperature (T_v) and compressibility
 381 (β_f) at varying relative amplitude of pore pressure oscillations ($P_r = 0.1$ to 0.8). At fixed
 382 P_r , both S_b and ρ_b decrease with increasing T_v and hence β_f . Furthermore, S_b and ρ_b decrease
 383 with increasing P_r at fixed T_v and β_f . Note that the results are clipped at $\rho_b = 1000 \text{ kg/m}^3$,
 384 which is the presumed maximum density of the rising brine within the discharge zone (see discussion
 385 in Section 4.3).

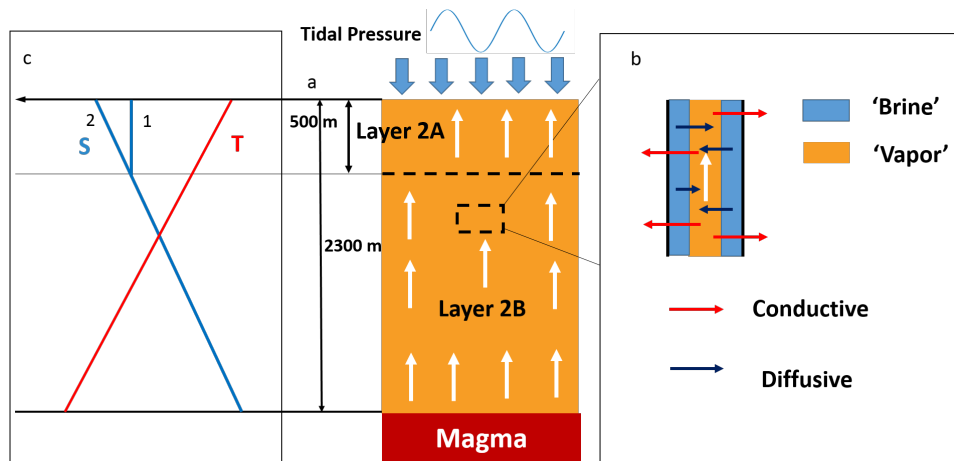


386 **Figure 9.** Estimated brine properties from decoupled temperature and chlorinity tidal oscillations:
 387 chlorinity (top) and density (bottom) as functions of vapor temperature (T_v)/compressibility (β_f) and relative
 388 amplitude of pore pressure oscillations (P_r). The results are cropped at the presumed maximum brine density
 389 of 1000 kg/m^3 .

390 According to Figure 9, the brine properties required to explain the tidal oscillations in
391 chloride are $T_b = 380$ to 400 °C and $S_b = 6485$ to 2280 mmol/kg. Note that the maximum
392 of S_b is within the range of the model predicted chlorinity (30 to 50 Wt.% or 5133 to 8556
393 mmol/kg) of the end-member brine formed in the basal reaction zone [*Choi and Lowell, 2015*],
394 which suggests minimal alteration of the end-member brine after it leaves its point of origin.
395 On the other hand, the lower values of S_b point to dilution of the end-member brine by less-
396 saline pore fluids during ascent and prior to tidally driven mixing with 'vapor'.

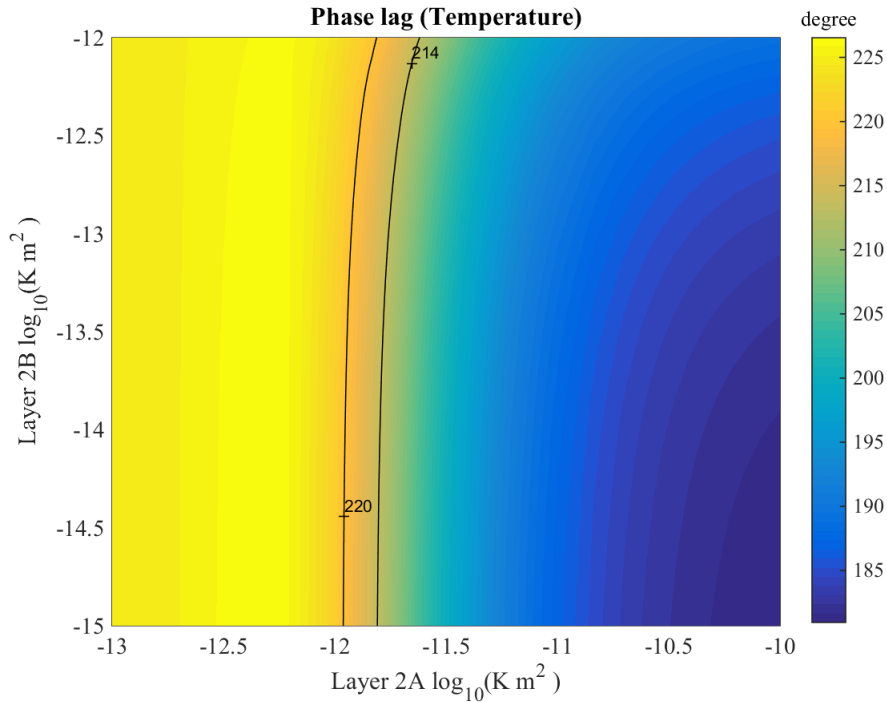
397 **4.5 Coupled Tidal Oscillations of Temperature and Chlorinity from Subsurface Tidal** 398 **Pumping**

399 The conceptual model of the storage of brine within the discharge zone of a hydrothermal
400 circulation cell (whereby brine preferentially fills small fissures, dead ends, and covers the inner
401 walls of the main conduit through which the vapor flows [*Fontaine and Wilcock, 2006*]) should
402 allow another explanation for the tidal oscillations in venting chlorinity. As illustrated in Figure
403 10, if the inner walls of the main conduits through which the vapor rises are covered by brine,
404 then chloride will be transferred from brine to vapor through diffusion. Such diffusion will cause
405 the chlorinity of a vapor parcel rising through the conduit to increase gradually and thus leads
406 to a vertical chlorinity gradient along the discharge zone. Unlike the vertical temperature gradient
407 caused by conductive and adiabatic heat loss, which can persist through out the discharge zone,
408 the chlorinity gradient may only exist within layer 2B assuming a permeability contrast between
409 layer 2A and 2B. According to *Fontaine and Wilcock [2006]*, when layer 2A has much larger
410 permeability than layer 2B, the vertical pressure gradient driving the upflow in layer 2A is much
411 smaller than the pressure gradient in layer 2B. As a result, the rising brine becomes negatively
412 buoyant after it crosses the interface and ultimately starts sinking. In this case, the storage of
413 brine occurs only in layer 2B such that the vertical gradient of 'vapor' chlorinity does not extend
414 beyond the 2A/2B contrast (Figure 10c2). Alternatively, when layer 2A and 2B have comparable
415 permeabilities, the storage of brine will persist through out the discharge zone as will the vertical
416 gradient of vapor chlorinity (Figure 10c1).



417 **Figure 10.** Schematic of the formation of temperature and chlorinity gradients along the hydrothermal
 418 discharge zone. The temperature gradient forms as a result of the conductive and adiabatic cooling of the
 419 rising vapor. The chlorinity gradient forms as a result of the diffusion of chloride from brine to vapor within
 420 the major conduits. Unlike the temperature gradient that persists throughout the discharge zone, the chlorinity
 421 gradient may end at the layer 2A/2B interface because of the absence of brine storage in layer 2A when the
 422 crustal permeability of layer 2A is much larger than that of layer 2B (case 1). Alternatively, the chlorinity
 423 gradient can persist throughout the discharge zone as the temperature gradient when the crustal permeability
 424 of layer 2A is similar to that of layer 2B (case 2).

425 If vertical temperature and chlorinity gradients exist along the discharge zone, then *the*
426 *mechanism of subsurface tidal pumping can lead to coupled tidal oscillations in venting temperature*
427 *and chlorinity*. Under tidal loading, the flow rate of the rising vapor will oscillate at tidal frequencies
428 driven by the oscillating pore pressure gradient. Such oscillating flow velocity causes displacement
429 of the vertical temperature and chlorinity gradients, which then causes the temperature and chlorinity
430 of the vapor at a given depth to vary at tidal frequencies. Theoretically, we can estimate the
431 phase-lag of temperature relative to tidal loading at the seafloor from the pore pressure variations
432 predicted by the two-layer poroelastic model (Section 4.2) using the formulas adapted from
433 the ones given in *Jupp and Schultz* [2004b] (Appendix B). According to Figure 11, for M2 tide,
434 the phase lag of venting temperature decreases with increasing layer 2A permeability and is
435 relatively insensitive to layer 2B permeability. The layer 2A permeability corresponding to the
436 observed phase lag has a mean value of $1.5 \times 10^{-12} \text{ m}^2$ (contour lines in Figure 11). Note
437 that this estimate is approximately one order of magnitude higher than that obtained by *Barreyre*
438 *and Sohn* [2016] ($2.5 \times 10^{-13} \text{ m}^2$) based on the single-layer simplification of the poroelastic formulas
439 given in Appendices A and B. In their model, the impermeable bottom boundary is set at the
440 layer 2A/2B interface, which is essentially comparable to our two-layer model with very small
441 layer 2B crustal permeability (i.e., the lower ends of the contour lines in Figure 11). The discrepancy
442 is due to the large difference between the fluid compressibility applied. In the current study,
443 the fluid compressibility is calculated using the equation of state developed by *Driesner* [2007]
444 for 370 °C 2.85 Wt.% (489 mmol/kg) NaCl solution at a reference pressure of 3.35×10^4
445 kPa. The result: $\beta_f = 5.3 \times 10^{-9} \text{ Pa}^{-1}$ is an order of magnitude higher than the one used
446 by *Barreyre and Sohn* [2016]: $\beta_f = 4.8 \times 10^{-10} \text{ Pa}^{-1}$, which is relatively low for high temperature
447 pore fluids.



448 **Figure 11.** Phase lag of venting temperature relative to M2 tide predicted by the poroelastic model. The
 449 contours lines mark the lower and upper limit of the observed phase lag.

450 For venting chlorinity, when layer 2A/2B have comparable permeabilities (close to the
 451 upper ends of the contour lines in Figure 11), the storage of brine and thus the vertical gradient
 452 of vapor chlorinity are expected to persist throughout the discharge zone. In this case, we can
 453 estimate the phase lag of venting chlorinity in the same manner as temperature (see Appendix
 454 B for the formulas used). The results suggest venting chlorinity is essentially out of phase (i.e.,
 455 lagging by 180° with deviation < 0.15°) with venting temperature across the entire range of
 456 the layer 2A/2B crustal permeabilities applied, which is expected because the vertical gradients
 457 of chlorinity and temperature have opposite signs with temperature increasing and chlorinity
 458 decreasing with depth. This prediction is also close to the observed phase lag between venting
 459 chlorinity and temperature: $204 \pm 16^\circ$ (Table 3).

460 When layer 2A has much larger permeability than layer 2B (close to the lower ends of
 461 the contour lines in Figure 11), the storage of brine only occurs in layer 2B and the vertical
 462 gradient of vapor ends at the layer interface (Figure 10c2). As a result, the tidal phase of chlorinity
 463 observed at the seafloor should be the tidal phase at the interface plus what is associated with
 464 the time taken by the vapor to reach the seafloor or the residence time of high-temperature hydrothermal

465 fluid in layer 2A. The latter is dependent on the interstitial upflow velocity within layer 2A.
 466 In this study, we assume the upflow velocity is uniform throughout the discharge zone and obtain
 467 an estimate as (Appendix B):

$$w = \frac{Q}{\rho_v A \phi} \quad (5)$$

468 where w is the interstitial upflow velocity, $Q = 292$ kg/s is the estimated mass flux within
 469 the discharge zone beneath the MEF [Lowell *et al.*, 2013], $\rho_v = 646$ kg/m³ is the vapor density,
 470 A is the area of the horizontal cross-section of the upper discharge zone in layer 2A, which
 471 is assumed to equal the area of the vent field: 6×10^4 m² [Lowell *et al.*, 2013], and $\phi = 0.2$
 472 is the crustal porosity of layer 2A [Crone and Wilcock, 2005]. The result: $w = 3.8 \times 10^{-5}$
 473 m/s suggests it will take approximately 154 days for the vapor to rise through the 500-m thick
 474 layer 2A. Such a residence time is likely an overestimate since w is calculated assuming the
 475 area of the horizontal cross-section of the discharge zone in layer 2A equals the area of the
 476 entire vent field. In order to shorten the residence time to the period of M2 tide (~ 0.5 day),
 477 the area of the horizontal cross-section of the discharge zone needs to be smaller than 1% of
 478 the area of the vent field. Either way, the tidal phase of venting chlorinity is poorly constrained
 479 because of the large uncertainty in the upflow residence time in layer 2A.

480 5 Discussion

481 5.1 Hypothesis Test Results

482 As for the first hypothesis, according to the discussion in Section 4.3, interpreting the
 483 observed tidal oscillations in temperature and chloride as a result of subsurface mixing alone
 484 requires the vapor to be highly compressible: $\beta_f > 1.9 \times 10^{-7}$ Pa⁻¹. This lower limit of
 485 β_f is within the range of the estimated β_f for near-critical water [Johnson and Norton, 1991],
 486 whose compressibility goes to infinity at its critical point. However, for a NaCl solution, the
 487 maximum compressibility is finite and decreases dramatically with increasing chlorinity. According
 488 to Klyukin *et al.* [2016], the maximum of β_f for a NaCl solution with the same chlorinity as
 489 the vapor (2.85 Wt.%) is 6.7×10^{-8} Pa⁻¹, which is approximately a third of the minimum
 490 compressibility required to explain the coupled temperature and chloride tidal oscillations. In
 491 addition, according to Figure 8(a), the estimated brine temperature is at least 48 °C lower than
 492 the vapor temperature (400 °C). It is questionable such a sharp thermal gradient can exist given
 493 the close proximity between brine and vapor in the hypothesized sub-seafloor layout (Figure

494 3), whereby thermal conduction is likely to homogenize any temperature difference and lead
 495 to thermal equilibrium between brine and vapor. The arguments above thus invalidate the first
 496 hypothesis, which is subsurface tidal mixing causes coupled tidal oscillations in venting temperature
 497 and chlorinity.

498 As for the second hypothesis, comparing the results shown in Figure 9 with 8, the requirement
 499 for highly-compressible near-critical vapor is relaxed in the case of decoupled temperature and
 500 chlorinity oscillations. The minimum compressibility required to explain chloride oscillations
 501 alone is $\beta_f \sim 1 \times 10^{-8} \text{ Pa}^{-1}$ at $P_r = 0.8$. This minimum increases to $4 \times 10^{-8} \text{ Pa}^{-1}$ at
 502 $P_r = 0.14$. Those values are both below the estimated maximum compressibility of $6.7 \times$
 503 10^{-8} Pa^{-1} for near-critical vapor [Klyukin *et al.*, 2016]. As a result, when P_r is high, which
 504 corresponds to large crustal permeabilities (e.g., $P_r = 0.8$ corresponds to $K = 9.1 \times 10^{-11} \text{ m}^2$
 505 for layer 2A and $K = 9.1 \times 10^{-13} \text{ m}^2$ for layer 2B), the requirement for near-critical vapor
 506 is lifted and thus the mixing is no-longer restricted to the depth corresponding to the critical
 507 pressure of the vapor (e.g., $2.9 \times 10^4 \text{ kPa}$). Therefore, instead of being limited to a thin vertical
 508 layer, as presumed in deriving the results shown in Figure 9, the mixing process can occur over
 509 a relative broad segment of the discharge zone where brine is stored and the tidally driven subsurface
 510 pore pressure change is significant.

511 As for the third hypothesis, that subsurface tidal pumping causes coupled tidal oscillations
 512 in venting temperature and chlorinity, the results shown in Section 4.5 suggest, as predicted
 513 by the poroelastic model, the phase angle of the M2 tidal oscillations in venting temperature
 514 correspond to the layer 2A crustal permeability of $\sim 1.5 \times 10^{-12} \text{ m}^2$. This value falls into
 515 the range of the previous estimates (10^{-10} to 10^{-13} m^2). In addition, the phase lag between
 516 the tidal oscillations in temperature and chlorinity predicted by the poroelastic model ($\sim 180^\circ$)
 517 is close to the observation ($204 \pm 16^\circ$) in the case of layer 2A and 2B having similar permeabilities.
 518 When the permeability of layer 2A is much larger than that of layer 2B, the phase lag is poorly
 519 constrained.

520 In summary, the discussion above suggests the first hypothesis is unlikely to be the causal
 521 mechanism for the tidal oscillations of hydrothermal venting at Grotto, while the second and
 522 third hypotheses can both potentially explain the observation. The current model prediction
 523 and observational data are inadequate to determine which one is the dominant mechanism.

524 **5.2 Limitations of 1-D Poroelastic Model**

525 In this study, the one-dimensional poroelastic model used to estimate the incremental
526 pore pressure assumes single-phase fluid (vapor) with uniform properties. In reality, the presence
527 of brine and spatial variations of fluid properties will introduce additional uncertainty into the
528 pore pressure predicted by the model. In addition, since the model is one dimensional, it excludes
529 lateral pressure gradients and interstitial flows. However, 2-D numerical simulations suggest
530 tidal loading can result in lateral pressure gradients that drive horizontal flows into and out of
531 the discharge zone of a hydrothermal circulation cell [Crone and Wilcock, 2005]. The horizontal
532 pressure gradient is a result of the lateral contrast of crustal and pore fluid properties across
533 the interface between the focused hydrothermal discharge zone and its host formation. Those
534 different crustal and fluid properties lead to different poroelastic response to tidal loading and
535 hence lateral pore pressure gradient and interstitial flows across the interface. The presence
536 of horizontal flows into and out of the discharge zone causes its pore pressure and vertical interstitial
537 flow variations to deviate from those predicted by the 1-D model and thus introduces additional
538 uncertainty into the results presented in this paper. More importantly, the tidally-driven horizontal
539 interstitial flows can drive mixing of pore fluids with contrasting temperature and chlorinity
540 between the discharge zone and its surroundings, which, by itself, can potentially result in the
541 observed tidal variations of venting temperature and chlorinity. To test this hypothesis and better
542 understand subsurface fluid flows and their influences on seafloor venting requires developing
543 a 2-D poroelastic model with both two-phase fluids [Choi and Lowell, 2015] and seafloor tidal
544 loading [Crone and Wilcock, 2005] that accounts for the lateral heterogeneity of crustal and
545 fluid properties, which will be a goal for future research.

546 **6 Conclusions**

547 This study tests three hypothetical scenarios in which seafloor pressure loading can lead
548 to tidal modulations of venting temperature and chlorinity at the Grotto mound through subsurface
549 tidal mixing and/or subsurface tidal pumping. The results suggest it is unlikely for subsurface
550 tidal mixing to cause coupled tidal oscillations of the observed amplitudes in venting temperature
551 and chlorinity. It is possible that the tidal oscillations in venting temperature and chlorinity
552 are decoupled with subsurface tidal pumping causing the temperature variations and subsurface
553 tidal mixing causing the chlorinity variations, although the mixing depth is not well constrained.
554 Finally, it is plausible for subsurface tidal pumping to cause coupled tidal oscillations in venting
555 temperature and chlorinity. In this case, the observed tidal phase lag between venting temperature

556 and chlorinity is close to the poroelastic model prediction if the brine storage occurs throughout
 557 the upflow zone under the premise that layer 2A and 2B have similar crustal permeabilities.
 558 On the other hand, the phase lag is poorly constrained if the brine storage is limited to layer
 559 2B when its crustal permeability is much smaller than that of layer 2A. Last but not least, the
 560 results summarized above are preliminary due to the complexity of seafloor hydrothermal
 561 circulation that is unaccounted for by the simplified 1-D poroelastic model applied. Likewise,
 562 the analysis in this paper is insufficient to rule out other mechanisms, such as lateral mixing
 563 of pore fluid between discharge zone and surroundings (Section 5.2), as the cause of the observed
 564 tidal signals in venting temperature and chlorinity. A more realistic way to investigate the poroelastic
 565 response of hydrothermal circulation to tidal loading and a goal for future research will be to
 566 develop a 2-D poroelastic model with two-phase fluids and seafloor loading.

567 **A: Two-layer Poroelastic Model Formulas**

568 According to the theory of poroelasticity, under seafloor tidal loading, the pore pressure
 569 perturbation (\hat{P}) comprises an instantaneous component (\hat{P}_i) that is invariant with depth and
 570 a flow-induced diffusive component (\hat{P}_d) that propagates from the seafloor into the crustal formation
 571 and from the formation layer interfaces into internal layers [*Wang and Davis, 1996; Jupp and*
 572 *Schultz, 2004b*]. Between the two components, \hat{P}_i is in phase with the loading tide while \hat{P}_d
 573 is lagging with a phase angle dependent on the tidal period along with crustal and fluid properties.

574 According to *Wang and Davis [1996]*, the pore pressure perturbation within each layer
 575 of the one-dimensional crustal formation illustrated in Figure 3 is governed by the following
 576 equation:

$$\frac{\partial \hat{P}_j}{\partial t} - \frac{k_j}{\mu_j \Sigma_j} \frac{\partial^2 \hat{P}_j}{\partial z^2} = \gamma_j \frac{\partial \sigma_P}{\partial t}, \quad (\text{A.1})$$

577 where the subscript j denotes properties in layer 2A: $j = 1$ and layer 2B: $j = 2$, μ is dynamic
 578 viscosity, Σ and γ are the one-dimensional storage compressibility and Skempton ratio respectively
 579 [*Jupp and Schultz, 2004b*], and $\sigma_P = A_P \exp(i\Omega t)$ is the loading tidal harmonic having amplitude
 580 A_P and angular frequency Ω . In practice, we estimate dynamic viscosity as a function of fluid
 581 temperature as $\mu = C_1/(C_2 + T_f)$, where $T_f = 370^\circ\text{C}$, $C_1 = 0.032 \text{ Pas}/^\circ\text{C}$, and $C_2 =$
 582 15.4°C [*Germanovich et al., 2000*]. We calculate Σ and γ using the formulas given in *Jupp*
 583 *and Schultz [2004b]* and the typical values of layer 2A/2B crustal properties given in *Crone*

584 *and Wilcock* [2005]. The solution to equation (A.1) can be decoupled into instantaneous and
 585 diffusive components

$$\hat{P}_j = \hat{P}_{ij} + \hat{P}_{dj}, \quad (\text{A.2})$$

586 which satisfy the governing equations [*Wang and Davis*, 1996]

$$\hat{P}_{ij} = \gamma_j \sigma_P, \quad (\text{A.3})$$

$$\frac{\partial \hat{P}_{dj}}{\partial t} = \frac{k_j}{\mu_j \Sigma_j} \frac{\partial^2 \hat{P}_{dj}}{\partial z^2}. \quad (\text{A.4})$$

587 In practice, equation (A.4) is solved with the following boundary conditions. First, the
 588 seafloor is treated as an open boundary for fluid flow and thus at $z = 0$ m,

$$\hat{P}_1 = \hat{P}_{i1} + \hat{P}_{d1} = \sigma_P. \quad (\text{A.5})$$

589 At layer 2A/2B interface ($z = -h = -500$ m), the continuity of pore pressure and Darcy
 590 fluid velocity requires

$$\hat{P}_{d1} + \gamma_1 \sigma_P = \hat{P}_{d2} + \gamma_2 \sigma_P, \quad (\text{A.6})$$

$$\frac{k_1}{\mu_1} \frac{\partial \hat{P}_{d1}}{\partial z} = \frac{k_2}{\mu_2} \frac{\partial \hat{P}_{d2}}{\partial z}. \quad (\text{A.7})$$

591 The bottom boundary of layer 2B is treated as impermeable to fluid flows and thus at $z =$
 592 $-H = -2300$ m

$$\frac{k_2}{\mu_2} \frac{\partial \hat{P}_{d2}}{\partial z} = 0. \quad (\text{A.8})$$

593 Assuming the solution to equation (A.4) has the following form

$$\hat{P}_{dj} = C_j(z) \exp(i\Omega t), \quad (\text{A.9})$$

594 substituting into equation (A.4) gives

$$i\Omega C_j = \frac{k_j}{\mu_j \Sigma_j} \frac{\partial^2 C_j}{\partial z^2}. \quad (\text{A.10})$$

595 The solution to equation (A.10) has the form

$$C_j(z) = a_j \exp(\Psi_j z) + b_j \exp(-\Psi_j z) \quad (\text{A.11})$$

596 where $\Psi = \sqrt{i\Omega\mu_j\Sigma_j/k_j}$ and a_j, b_j are constant coefficients. Substituting (A.11) into the
 597 boundary conditions (A.5) to (A.8) leads to a system of four equations that is solved for $a_1,$
 598 b_1, a_2, b_2 . The values of the constant parameters used are given in Table 2.

599 **B: Temperature and Chlorinity Variations from Subsurface Tidal Pumping**

600 This section gives the the formulas used to calculate the phase lags of venting temperature
 601 and chlorinity relative to ocean tide from the pore pressure variations predicted by the poroelastic
 602 model described in Appendix A. As discussed in Section 4.5, the conductive and adiabatic cooling
 603 causes the temperature of vapor to decrease as it rises through the subsurface discharge zone.
 604 In the meantime, the chlorinity of vapor increases as a result of the diffusion of chloride from
 605 brine to vapor inside a major conduit (Figure 10). We thus assume the steady-state vapor temperature
 606 and chlorinity to be

$$\bar{T}_v = \bar{T}_{v0} - \Gamma_T z, \quad (\text{B.1})$$

$$\bar{S}_v = \bar{S}_{v0} + \Gamma_S z. \quad (\text{B.2})$$

607 where T_{v0} and S_{v0} are the steady-state temperature and chlorinity at the seafloor; Γ_T and $\Gamma_S,$
 608 both of which are positive constants, are the steady-state gradients.

609 Assuming thermal equilibrium between the rising vapor and the bounding rock, then the
 610 steady-state vertical advection speed for temperature signals can be estimated as

$$\bar{w}_T = \frac{Q}{\rho_v A} \quad (\text{B.3})$$

611 where $Q = 292$ kg/s is the estimated mass flux within the discharge zone beneath the MEF
 612 [Lowell *et al.*, 2013], $\rho_v = 646$ kg/m³ is vapor density, and $A = 6 \times 10^4$ m² is the area of
 613 horizontal cross-section of discharge zone, which is assumed to equal the area of the vent field.
 614 In the meantime, the chlorinity signals are advected at the speed of interstitial flows, which
 615 is related to \bar{w}_T as

$$\bar{w}_S = \frac{\bar{w}_T}{\phi} \quad (\text{B.4})$$

616 where ϕ is crustal porosity.

617 Under tidal loading, the temperature, chlorinity and the advection speeds can be written

618 as

$$T_v = \bar{T}_v + \hat{T}_v, \quad (\text{B.5})$$

$$S_v = \bar{S}_v + \hat{S}_v, \quad (\text{B.6})$$

$$w_T = \bar{w}_T + \hat{w}_T, \quad (\text{B.7})$$

$$w_S = \bar{w}_S + \hat{w}_S, \quad (\text{B.8})$$

619 where the second terms on the right hand sides represent tidally-induced perturbations, which
 620 are assumed to be much smaller than the steady-state terms. When neglecting adiabatic cooling
 621 and the tidally-induced perturbation in fluid density, the conservation of energy for the rising
 622 vapor along the discharge zone can be expressed as [Jupp and Schultz, 2004b]:

$$\frac{\partial}{\partial t}(\bar{T}_v + \hat{T}_v) + (\bar{w}_T + \hat{w}_T) \frac{\partial}{\partial z}(\bar{T}_v + \hat{T}_v) = -\Gamma_T \bar{w}_T. \quad (\text{B.9})$$

623 Similarly, the conservation of chloride equation can be written as

$$\frac{\partial}{\partial t}(\bar{S}_v + \hat{S}_v) + (\bar{w}_S + \hat{w}_S) \frac{\partial}{\partial z}(\bar{S}_v + \hat{S}_v) = \Gamma_S \bar{w}_S. \quad (\text{B.10})$$

624 We linearize equations (B.9) and (B.10) by substituting (B.1) and (B.2) for \bar{T}_v and \bar{S}_v and neglecting
 625 the second-order perturbation terms to get

$$\frac{\partial \hat{T}_v}{\partial t} + \bar{w}_T \frac{\partial \hat{T}_v}{\partial z} = \Gamma_T \hat{w}_T, \quad (\text{B.11})$$

$$\frac{\partial \hat{S}_v}{\partial t} + \bar{w}_S \frac{\partial \hat{S}_v}{\partial z} = -\Gamma_S \hat{w}_S. \quad (\text{B.12})$$

626 The advection speed perturbation for temperature is related to the tidally-induced incremental
 627 pore pressure by Darcy's law:

$$\hat{w}_T = -\frac{k}{\mu} \frac{\partial \hat{P}_d}{\partial z}. \quad (\text{B.13})$$

628 Again, since the chloride signals are advected at the speed of interstitial flows, we have

$$\hat{w}_S = \frac{1}{\phi} \hat{w}_T. \quad (\text{B.14})$$

629 Substituting equations (A.9) and (A.11) into (B.13) gives

$$\hat{w}_{Tj} = -\frac{k_j}{\mu_j} [a_j \Psi_j \exp(\Psi_j z) - b_j \Psi_j \exp(-\Psi_j z)] \exp(i\Omega t), \quad (\text{B.15})$$

630 and from equation (B.14):

$$\hat{w}_{Sj} = -\frac{k_j}{\mu_j \phi_j} [a_j \Psi_j \exp(\Psi_j z) - b_j \Psi_j \exp(-\Psi_j z)] \exp(i\Omega t). \quad (\text{B.16})$$

631 where subscript j denotes properties in layer 2A: $j = 1$ and layer 2B: $j = 2$.

632 In practice, we substitute equations (B.3) and (B.4) for \bar{w}_T and \bar{w}_S and equations (B.15)
 633 and (B.16) for \hat{w}_T and \hat{w}_S in equation (B.11) and (B.12). We then solve these two equations
 634 for \hat{T}_v and \hat{S}_v with the boundary conditions: $\hat{T}_v = \hat{S}_v = 0$ at the bottom boundary of layer
 635 2B ($z = -H = -2300$ m). Those boundary conditions are derived based on the assumption
 636 that the end-member vapor formed within the basal reaction zone has sufficient thermal and
 637 compositional inertia that the temperature and chlorinity are held constant under tidal loading.
 638 At layer 2A/2B interface, we assume continuity for temperature and chlorinity, which requires:
 639 $\hat{T}_{v1} = \hat{T}_{v2}$ and $\hat{S}_{v1} = \hat{S}_{v2}$ at $z = -h = -500$ m.

640 The solution to equations (B.11) and (B.12) have the following expressions:

$$\hat{T}_{vj} = \left\{ q_{Tj} \exp\left(-\frac{i\Omega}{\bar{w}_{Tj}} z\right) + m_{Tj} \exp(\Psi_j z) + n_{Tj} \exp(-\Psi_j z) \right\} \exp(i\Omega t), \quad (\text{B.17})$$

$$\hat{S}_{vj} = \left\{ q_{Sj} \exp\left(-\frac{i\Omega}{\bar{w}_{Sj}} z\right) + m_{Sj} \exp(\Psi_2 z) + n_{Sj} \exp(-\Psi_2 z) \right\} \exp(i\Omega t). \quad (\text{B.18})$$

641 The constant coefficients in equations (B.17) and (B.18) are:

$$m_{Tj} = -\frac{\Gamma_T k_j a_j \Psi_j}{\mu_j (\bar{w}_{Tj} \Psi_j + i\Omega)}, \quad (\text{B.19})$$

$$n_{Tj} = -\frac{\Gamma_T k_j b_j \Psi_j}{\mu_j (\bar{w}_{Tj} \Psi_j - i\Omega)}, \quad (\text{B.20})$$

$$q_{T2} = \frac{[-m_{T2} \exp(-\Psi_2 H) - n_{T2} \exp(\Psi_2 H)]}{\exp(i\Omega H / \bar{w}_{T2})}, \quad (\text{B.21})$$

$$q_{T1} = \frac{\left[\frac{\hat{T}_{v2}|_{z=-h}}{\exp(i\Omega t)} - m_{T1} \exp(-\Psi_1 h) - n_{T1} \exp(\Psi_1 h) \right]}{\exp(i\Omega h / \bar{w}_{T1})}, \quad (\text{B.22})$$

$$m_{Sj} = \frac{\Gamma_S k_j a_j \Psi_j}{\mu_j (\bar{w}_{Sj} \Psi_j + i\Omega)}, \quad (\text{B.23})$$

$$n_{Sj} = \frac{\Gamma_S k_j b_j \Psi_j}{\mu_j (\bar{w}_{Sj} \Psi_j - i\Omega)}, \quad (\text{B.24})$$

$$q_{S1} = \frac{\left[\frac{\hat{S}_{v2}|_{z=-h}}{\exp(i\Omega t)} - m_{S1} \exp(-\Psi_1 h) - n_{S1} \exp(\Psi_1 h) \right]}{\exp(i\Omega h / \bar{w}_{S1})}, \quad (\text{B.25})$$

$$q_{S2} = \frac{[-m_{S2} \exp(-\Psi_2 H) - n_{S2} \exp(\Psi_2 H)]}{\exp(i\Omega H / \bar{w}_{S2})}, \quad (\text{B.26})$$

642 where a_j and b_j are the constant coefficients in the solution of the diffusive pore pressure perturbation
643 (\hat{P}_d) (equation (A.11)).

644 Acknowledgments

645 G. Xu was funded by the Woods Hole Oceanographic Institution as a postdoctoral scholar. B.
646 I. Larson was partially funded by the PMEL Earth-Ocean Interactions Program and the Joint
647 Institute for the Study of the Atmosphere and Ocean (JISAO) under NOAA Cooperative Agreement
648 no. NA10OAR4320148. This is JISAO Contribution Number 2016-01-33, and PMEL Contribution
649 Number 4533. K. G. Bemis was funded by the National Science Foundation (NSF) award OCE-
650 1234141. The original development of the resistivity instruments was through an NSF grant
651 to M. Lilley (94069965). Additional NSF grants (9820105, 0120392, 0701196, 0751868, 0819004)
652 allowed improvements and field deployments to be made. Additional support from the W.M.
653 Keck Foundation is gratefully acknowledged. Funds to refurbish the instrument for the deployment
654 that produced the data discussed here were provided by ONC. We gratefully acknowledge the
655 ROPOS group along with Ian Kulin and Steve Mihaly for their efforts during the deployment.
656 We also gratefully acknowledge the efforts of Eric Olson through many years to help make
657 these instruments field ready. The temperature and resistivity data recorded by BARS can be
658 downloaded through the data search interface of ONC database (<http://dmas.uvic.ca/DataSearch>).

659 **References**

- 660 Barreyre, T., and R. A. Sohn, Poroelastic response of mid-ocean ridge hydrothermal
661 systems to ocean tidal loading: Implications for shallow permeability structure,
662 *Geophysical Research Letters*, *43*, doi:10.1002/2015GL066479, 2016.
- 663 Barreyre, T., J. Escartin, R. Sohn, and M. Cannat, Permeability of the lucky strike
664 deep-sea hydrothermal system: Constraints from the poroelastic response to
665 ocean tidal loading, *Earth and Planetary Science Letters*, *408*, 146 – 154, doi:
666 <http://dx.doi.org/10.1016/j.epsl.2014.09.049>, 2014a.
- 667 Barreyre, T., J. Escartín, R. A. Sohn, M. Cannat, V. Ballu, and W. C. Crawford, Temporal
668 variability and tidal modulation of hydrothermal exit-fluid temperatures at the lucky
669 strike deep-sea vent field, mid-atlantic ridge, *Journal of Geophysical Research*, *119*,
670 2543–2566, doi:10.1002/2013JB010478, 2014b.
- 671 Carlson, R. L., The effect of hydrothermal alteration on the seismic structure of the
672 upper oceanic crust: Evidence from holes 504b and 1256d, *Geochemistry, Geophysics,*
673 *Geosystems*, *12*(9), n/a–n/a, doi:10.1029/2011GC003624, q09013, 2011.
- 674 Choi, J., and R. P. Lowell, The response of two-phase hydrothermal systems to changing
675 magmatic heat input at mid-ocean ridges, *Deep-Sea Research Part II*, *121*, 17–30, 2015.
- 676 Clague, D. A., D. W. Caress, H. Thomas, D. Thompson, M. Calarco, J. Holden, and
677 D. Butterfield, Abundance and distribution of hydrothermal chimneys and mounds on
678 the Endeavour Ridge determined by 1-m resolution AUV multibeam mapping surveys,
679 *EOS, Transactions, American Geophysical Union*, *89*, Fall Meet. Suppl. abstr. V41B-
680 2079, 2008.
- 681 Clague, D. A., et al., Eruptive and tectonic history of the Endeavour Segment, Juan de
682 Fuca Ridge, based on AUV mapping data and lava flow ages, *Geochemistry Geophysics*
683 *Geosystems*, *15*, 3364–3391, doi:10.1002/2014GC005415, 2014.
- 684 Coogan, L. A., Reconciling temperatures of metamorphism, fluid fluxes, and heat transport
685 in the upper crust at intermediate to fast spreading mid-ocean ridges, *Geochemistry,*
686 *Geophysics, Geosystems*, *9*(2), n/a–n/a, doi:10.1029/2007GC001787, q02013, 2008.
- 687 Coumou, D., T. Driesner, P. Weis, and C. A. Heinrich, Phase separation, brine formation,
688 and salinity variation at black smoker hydrothermal systems, *Journal of Geophysical*
689 *Research: Solid Earth*, *114*(B3), n/a–n/a, doi:10.1029/2008JB005764, b03212, 2009.
- 690 Crone, T. J., and W. S. D. Wilcock, Modeling the effects of tidal loading on mid-
691 ocean ridge hydrothermal systems, *Geochemistry Geophysics Geosystems*, *6*, doi:

- 692 10.1029/2004GC000905, 2005.
- 693 Crone, T. J., W. S. D. Wilcock, and R. E. McDuff, Flow rate perturbations in a black
694 smoker hydrothermal vent in response to a mid-ocean ridge earthquake swarm,
695 *Geochemistry Geophysics Geosystems*, *11*, doi:10.1029/2009GC002926, 2010.
- 696 Davis, E. E., K. Wang, K. Becker, and R. E. Thomson, Formation-scale hydraulic and
697 mechanical properties of oceanic crust inferred from pore pressure response to periodic
698 seafloor loading, *Journal of Geophysical Research: Solid Earth*, *105*(B6), 13,423–13,435,
699 doi:10.1029/2000JB900084, 2000.
- 700 Davis, E. E., K. Wang, R. E. Thomson, K. Becker, and J. F. Cassidy, An episode of
701 seafloor spreading and associated plate deformation inferred from crustal fluid pressure
702 transients, *Journal of Geophysical Research: Solid Earth*, *106*(B10), 21,953–21,963,
703 doi:10.1029/2000JB000040, 2001.
- 704 Driesner, T., The system H₂O—NaCl. Part II: Correlations for molar volume, enthalpy,
705 and isobaric heat capacity from 0 to 1000 °C, 1 to 5000 bar, and 0 to 1 X_{NaCl} ,
706 *Geochimica et Cosmochimica Acta*, *71*, 4902–4919, doi:10.1016/j.gca.2006.01.033,
707 2007.
- 708 Driesner, T., and C. A. Heinrich, The system H₂O—NaCl. Part I: Correlation formulae
709 for phase relations in temperature-pressure-composition space from 0 to 1000 °C, 0
710 to 5000 bar, and 0 to 1 X_{NaCl}, *Geochimica et Cosmochimica Acta*, *71*, 4880–4901,
711 doi:10.1016/j.gca.2006.01.033, 2007.
- 712 Fontaine, F. J., and W. S. D. Wilcock, Dynamics and storage of brine in mid-ocean ridge
713 hydrothermal systems, *Journal of Geophysical Research: Solid Earth*, *111*(B6), n/a–n/a,
714 doi:10.1029/2005JB003866, b06102, 2006.
- 715 Germanovich, L. N., R. P. Lowell, and D. K. Astakhov, Stress-dependent permeability and
716 the formation of seafloor event plumes, *Journal of Geophysical Research-Solid Earth*,
717 *105*(B4), 8341–8354, doi:10.1029/1999jb900431, 2000.
- 718 Hearn, C. K., K. L. Homola, and H. P. Johnson, Surficial permeability of the axial
719 valley seafloor: Endeavour segment, Juan de Fuca ridge, *Geochemistry, Geophysics,*
720 *Geosystems*, *14*(9), 3409–3424, doi:10.1002/ggge.20209, 2013.
- 721 Johnson, J. W., and D. Norton, Critical phenomena in hydrothermal systems: state,
722 thermodynamic, electrostatic, and transport properties of H₂O in the critical region,
723 *American Journal of Science*, *291*, doi:10.2475/ajs.291.6.541, 1991.

- 724 Jupp, T. E., and A. Schultz, A thermodynamic explanation for black smoker temperatures,
725 *Nature*, 403, doi:10.1038/35002552, 2000.
- 726 Jupp, T. E., and A. Schultz, Physical balances in subseafloor hydrothermal convection
727 cells, *Journal of Geophysical Research*, 109, doi:10.1029/2003JB002697, 2004a.
- 728 Jupp, T. E., and A. Schultz, A poroelastic model for the tidal modulation of seafloor
729 hydrothermal systems, *Journal of Geophysical Research-Solid Earth*, 109(B3), doi:
730 10.1029/2003jb002583, 2004b.
- 731 Kelley, D. S., J. R. Delaney, and S. Kim Juniper, Establishing a new era of submarine
732 volcanic observatories: Cabling Axial Seamount and the Endeavour Segment of the
733 Juan de Fuca Ridge, *Marine Geology*, 352, 426–450, 2014.
- 734 Klyukin, Y., T. Driesner, M. Steele-MacInnis, R. Lowell, and R. J. Bodnar, Effect of
735 salinity on mass and energy transport by hydrothermal fluids based on the physical and
736 thermodynamic properties of H₂O–NaCl, *Geofluids*, pp. n/a–n/a, doi:10.1111/gfl.12181,
737 2016.
- 738 Larson, B. I., Watching the world sweat: Development and utilization of an in-situ
739 conductivity sensor for monitoring chloride dynamics in high temperature hydrothermal
740 fluids at divergent plate boundaries, Ph.D. thesis, University of Washington, 2008.
- 741 Larson, B. I., E. J. Olson, and M. D. Lilley, In situ measurement of dissolved chloride
742 in high temperature hydrothermal fluids, *Geochimica et Cosmochimica Acta*, 71, 2510–
743 2523, doi:10.1016/j.gca.2007.02.013, 2007.
- 744 Larson, B. I., M. D. Lilley, and E. J. Olson, Parameters of subsurface brines and
745 hydrothermal processes 12–15 months after the 1999 magmatic event at the Main
746 Endeavor Field as inferred from in situ time series measurements of chloride and
747 temperature, *Journal of Geophysical Research*, 114, doi:10.1029/2008JB005627, 2009.
- 748 Little, S. A., K. D. Stolzenbach, and F. J. Grassle, Tidal current effects on temperature in
749 diffuse hydrothermal flow: Guaymas basin, *Geophysical Research Letters*, 15, 1491–
750 1494, 1988.
- 751 Lowell, R. P., A. Farough, J. Hoover, and K. Cummings, Characteristics of magma-
752 driven hydrothermal systems at oceanic spreading centers, *Geochemistry Geophysics
753 Geosystems*, 14(6), 1756–1770, doi:10.1002/Ggge.20109, 2013.
- 754 Nedimovi, M. R., S. M. Carbotte, J. B. Diebold, A. J. Harding, J. P. Canales, and G. M.
755 Kent, Upper crustal evolution across the Juan de Fuca ridge flanks, *Geochemistry,
756 Geophysics, Geosystems*, 9(9), n/a–n/a, doi:10.1029/2008GC002085, q09006, 2008.

- 757 Nees, H. A., R. A. Lutz, T. M. Shank, and G. W. L. III, Pre- and post-eruption diffuse
758 flow variability among tubeworm habitats at 950 north on the east pacific rise, *Deep*
759 *Sea Research Part II: Topical Studies in Oceanography*, 56(1920), 1607 – 1615, doi:
760 <http://dx.doi.org/10.1016/j.dsr2.2009.05.007>, marine Benthic Ecology and Biodiversity:
761 A Compilation of Recent Advances in Honor of J. Frederick Grassle, 2009.
- 762 Newman, K. R., M. R. Nedimovi, J. P. Canales, and S. M. Carbotte, Evolution of
763 seismic layer 2b across the juan de fuca ridge from hydrophone streamer 2-d
764 travelttime tomography, *Geochemistry, Geophysics, Geosystems*, 12(5), n/a–n/a, doi:
765 10.1029/2010GC003462, q05009, 2011.
- 766 Ocean Networks Canada Data Archive, <http://www.oceannetworks.ca>, BARS resistivity
767 data from 1 Oct 2010 to 10 Feb 2014, Oceans Networks Canada, University of Victoria,
768 Canada. Downloaded on 17 Feb 2014, 2014a.
- 769 Ocean Networks Canada Data Archive, <http://www.oceannetworks.ca>, BARS temperature
770 data from 1 Oct 2010 to 10 Feb 2014, Oceans Networks Canada, University of Victoria,
771 Canada. Downloaded on 17 Feb 2014, 2014b.
- 772 Pawlowicz, R., B. Beardsley, and S. Lentz, Classical tidal harmonic analysis including
773 error estimates in MATLAB using T-TIDE, *Computer and Geosciences*, 28, 929–937,
774 2002.
- 775 Percival, D. B., and A. T. Walden, *Spectral Analysis for Physical Applications*, Cambridge
776 University Press, cambridge Books Online, 1993.
- 777 Scheirer, D. S., T. M. Shank, and D. J. Fornari, Temperature variations at diffuse and
778 focused flow hydrothermal vent sites along the northern east pacific rise, *Geochemistry,*
779 *Geophysics, Geosystems*, 7(3), n/a–n/a, doi:10.1029/2005GC001094, q03002, 2006.
- 780 Schultz, A., P. Dickson, and H. Elderfield, Temporal variations in diffuse hydrothermal
781 flow at TAG, *Geophysical Research Letters*, 23(23), 3471–3474, doi:10.1029/96gl02081,
782 1996.
- 783 Sohn, R. A., D. J. Fornari, K. L. V. Damm, J. A. Hildebrand, and S. C. Webb, Seismic
784 and hydrothermal evidence for a cracking event on the East Pacific Rise crest at 9
785 degrees 50 ' N, *Nature*, 396(6707), 159–161, doi:10.1038/24146, 1998.
- 786 Thomson, D. J., Spectrum estimation and harmonic analysis, *Proceedings of the IEEE*,
787 70(9), 1055–1096, doi:10.1109/PROC.1982.12433, 1982.
- 788 Tivey, M. K., A. M. Bradley, T. M. Joyce, and D. Kadko, Insights into tide-related
789 variability at seafloor hydrothermal vents from time-series temperature measurements,

790 *Earth Planetary Science Letters*, 202, 693–707, 2002.

791 Van Ark, E. M., et al., Seismic structure of the endeavour segment, juan de fuca ridge:

792 Correlations with seismicity and hydrothermal activity, *Journal of Geophysical*

793 *Research: Solid Earth*, 112(B2), n/a–n/a, doi:10.1029/2005JB004210, b02401, 2007.

794 Wang, K., and E. E. Davis, Theory for the propagation of tidally induced pore pressure

795 variations in layered subseafloor formations, *Journal of Geophysical Research: Solid*

796 *Earth*, 101(B5), 11,483–11,495, doi:10.1029/96JB00641, 1996.

797 Wilcock, W. S., and A. McNabb, Estimates of crustal permeability on the endeavour

798 segment of the juan de fuca mid-ocean ridge, *Earth and Planetary Science Letters*,

799 138(14), 83 – 91, doi:http://dx.doi.org/10.1016/0012-821X(95)00225-2, 1996.